

A conservative adaptive scheme for the 2D airfoil vortex interaction problem

D. Isola, A. Guardone and G. Quaranta*
Corresponding author: isola@aero.polimi.it

Politecnico di Milano, Dipartimento di Ingegneria Aerospaziale
Via La Masa 34, 20156 Milano, Italy

Abstract: In the present paper, preliminary computations for the vortex-airfoil interaction problem are shown. The Arbitrary Lagrangian-Eulerian formulation of the Euler equations is used to describe the fluid behaviour. An unsteady adaptive grid strategy is adopted to better capture the flow features, e.g. shock waves, and to reduce the numerical dissipation of the vortex.

Keywords: Adaptive Grids, Airfoil-Vortex Interaction, Arbitrary Lagrangian-Eulerian Formulation.

The computation of the dynamic loads over an airfoil caused by the interaction with external vortices is a challenging task. Numerical simulations of this kind of flow field are of interest since in rotorcrafts the blade-vortex interaction (BVI) could be a relevant source of noise and vibration [1]. The BVI phenomenon occurs when a rotor blade passes within a close proximity of the shed tip vortices from a previous blade. This causes a rapid, impulsive change in the pressure distribution along the blade resulting in the generation of highly directional impulsive loading noise. It has been shown that the main parameters governing the strength of a BVI are the distance between the blade and the vortex, termed miss-distance, the vortex strength at the time of the interaction, and how parallel or oblique the interaction is [2, 3]. The parallel BVI is the most critical configuration and occurs when the axis of the filament-like vortex is aligned with the axis of the blade.

Due to the high aspect-ratio of conventional blades a parallel BVI problem can generally be reduced to a two-dimensional airfoil-vortex interaction (AVI). This approach is ideal to study the underlying physical mechanisms involved in the interaction as it removes many of the complications of a three-dimensional BVI simulation and is computationally less expensive. One of the major challenges faced when simulating an AVI is to preserve the vortex structure accurately as it convects through the solution and minimize the numerical dissipation that is inherent in CFD simulations. Suitable techniques must be adopted to avoid the destruction of the vortices by the numerical dissipation [4, 5]. This is a well-known issue that arises when shock-capturing schemes are used to describe phenomena that have a linearly degenerate nature [6]. The work of Oh et al. [5] addressed this problem by the use of adaptive unstructured meshes to simulate a two-dimensional AVI. This method dynamically concentrates mesh points in region of large flow gradients, providing high resolution in the region of any vortices and other important flow features. Excellent results were achieved in this study and a similar approach has been adopted here.

In the present work the arbitrary Lagrangian-Eulerian (ALE) formulation of the Euler equations, in which the control volumes are allowed to change in shape and position as time evolves, is used to describe the behavior of the fluid. The governing equations are discretized resorting to a node centered finite-volume scheme in which the grid velocities are corrected to take into account the grid modifications performed by the adaptation scheme. [7, 8] The overall scheme allows to compute the solution at the current time level simply integrating the governing equations, without explicit interpolation of the solution, i.e. in a conservative manner. Moreover high order time integration schemes, e.g. standard BDF techniques, can be implemented very easily. [7, 8]

The ALE solver is briefly described in section 1 and the grid alteration strategy is introduced in section 2.

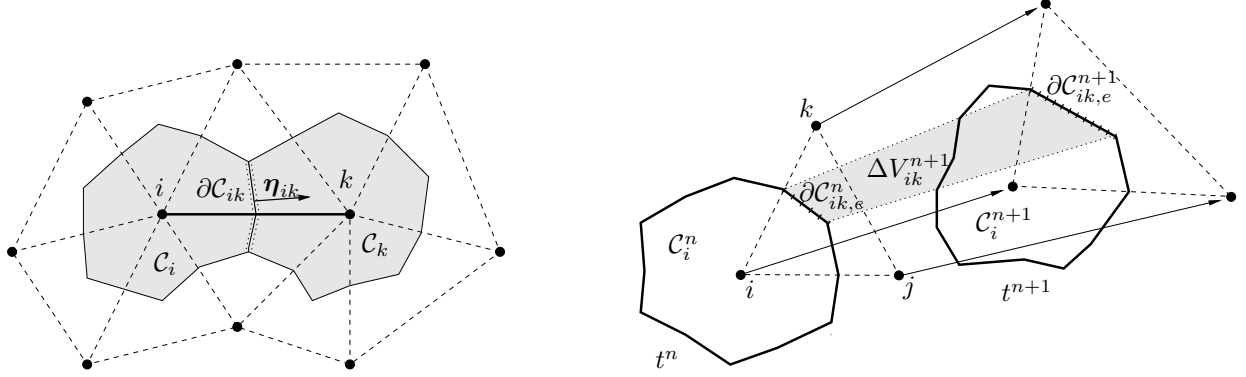


Figure 1: Left: edge associated with the finite volume interface $\partial\mathcal{C}_{ik} = \partial\mathcal{C}_i \cap \partial\mathcal{C}_k$ and metric vector $\boldsymbol{\eta}_{ik}$ in two spatial dimensions. The two shaded regions are the finite volumes \mathcal{C}_i and \mathcal{C}_k ; dashed lines indicate the underlying triangulation. Right: area swept by portion of the interface $\partial\mathcal{C}_{ik,e}$ pertaining to element e , made of nodes i, j and k , during the time interval $[t^n, t^{n+1}]$.

To better study the capabilities of the adaptive flow solver the simulation vortices transport within the flow field, the free-vortex advection problem is first tackled in section 3 on both fixed and adaptive grids. The airfoil-vortex interaction problem is presented in section 4.

1 Edge-Based Solver for Adaptive Grids

The Euler equations in an Arbitrary Lagrangian Eulerian (ALE) framework [9, 10] for compressible two-dimensional flows read

$$\frac{d}{dt} \int_{\mathcal{C}(t)} \mathbf{u} + \oint_{\partial\mathcal{C}(t)} [\mathbf{f}(\mathbf{u}) - \mathbf{u}\mathbf{v}] \cdot \mathbf{n} = 0, \quad \forall \mathcal{C}(t) \subseteq \Omega(t), \quad (1)$$

where $\mathcal{C}(t)$ is a closed subset of the domain $\Omega(t)$, $\partial\mathcal{C}(t)$ is the control volume boundary and \mathbf{n} is the outward unit vector. System (1) is made complete by specifying suitable initial and boundary conditions [11]. The flux function is defined as $\mathbf{f}(\mathbf{u}) = (\mathbf{m}, \mathbf{m} \otimes \mathbf{m}/\rho + P(\mathbf{u}) \mathbf{I}^2, [E^t + P(\mathbf{u})] \rho/\mathbf{m})^T$ and the term $\mathbf{u}\mathbf{v} = (\rho\mathbf{v}, \mathbf{m} \otimes \mathbf{v}, E^t\mathbf{v})^T$ accounts for the flux contribution due to the movement of the control volume. ρ is the density of mass, \mathbf{m} is the linear momentum vector, E^t is the total energy per unit volume, P is the local pressure, \mathbf{v} is the interface velocity and \mathbf{I}^2 is the 2×2 identity matrix.

The finite volume discrete counterpart of the Euler equation (1) is obtained by selecting a finite number of non overlapping volumes $\mathcal{C}_i(t) \subset \Omega(t)$. In the node-centered approach considered here, each cell surrounds a single node i of the triangulation of Ω , as shown in fig. 1. Over each finite volume, equation(1) reads

$$\frac{d[V_i \mathbf{u}_i]}{dt} = - \sum_{k \in \mathcal{K}_{i,\neq}} \int_{\partial\mathcal{C}_{ik}} [\mathbf{f}(\mathbf{u}) - \mathbf{u}\mathbf{v}] \cdot \mathbf{n} - \int_{\partial\mathcal{C}_i \cap \partial\Omega} [\mathbf{f}(\mathbf{u}) - \mathbf{u}\mathbf{v}] \cdot \mathbf{n}, \quad (2)$$

where $\mathbf{u}_i = \mathbf{u}_i(t)$ is the cell average of the unknown vector, V_i is the cell size. In equation (2) the sum is performed over the finite volumes \mathcal{C}_k that share a portion of their boundary with \mathcal{C}_i , i.e. $\partial\mathcal{C}_{ik} = \partial\mathcal{C}_i \cap \partial\mathcal{C}_k \neq \emptyset$, thus the set corresponding set of indexes is $\mathcal{K}_{i,\neq} = \{k \in \mathcal{K} : k \neq i | \partial\mathcal{C}_i \cap \partial\mathcal{C}_k \neq \emptyset\}$, see fig. 1. The second term of the right hand side of equation (2), i.e. $\partial\mathcal{C}_i \cap \partial\Omega$, is given by the boundary contribution, if any. Each contribution of equation (2) has to be approximated with a suitable integrated normal numerical flux, representing the exchange across the cell interface [6]. E.g. a centered approximation of the domain fluxes gives

$$\Phi(\mathbf{u}_i, \mathbf{u}_k, \nu_{ik}, \boldsymbol{\eta}_{ik}) = - \frac{\mathbf{f}(\mathbf{u}_i) + \mathbf{f}(\mathbf{u}_k)}{2} \cdot \boldsymbol{\eta}_{ik} + \frac{\mathbf{u}_i + \mathbf{u}_k}{2} \nu_{ik}, \quad (3)$$

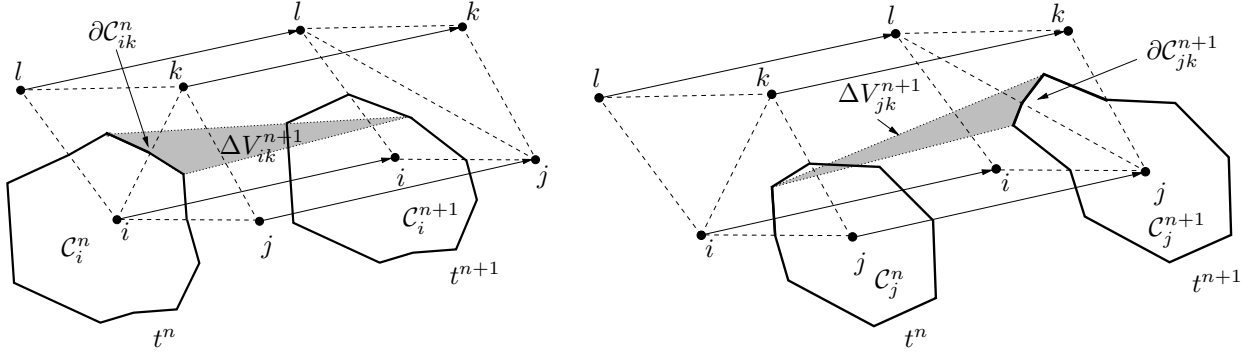


Figure 2: Interpretation of the edge swapping as continuous finite volume deformation. Left: evaluation of the normal interface velocity (area of the shaded region) for edge $i-k$ that is deleted due to edge-swapping from edge $i-k$ at time t^n into edge $j-k$ at time t^{n+1} . Right: evaluation of the normal interface velocity for edge $j-k$ that is created due to edge-swapping.

where the integrated normal vector and the integrated normal interface velocity are defined as

$$\boldsymbol{\eta}_{ik}(t) = \int_{\partial C_{ik}} \mathbf{n} \quad \text{and} \quad \nu_{ik}(t) = \int_{\partial C_{ik}} \mathbf{v} \cdot \mathbf{n}. \quad (4)$$

Equations (4)(left) and (4)(right) are consistency conditions that have to be exactly satisfied.

Moreover, by assuming a constant interface flux along the interface, the boundary integral in equation (2) simplifies to

$$\Phi^\partial(\mathbf{u}_i, \nu_i, \boldsymbol{\xi}_i) = -\mathbf{f}(\mathbf{u}_\partial(\mathbf{u}_i)) \cdot \boldsymbol{\xi}_i + \mathbf{u}_\partial(\mathbf{u}_i) \nu_i, \quad (5)$$

where the consistency conditions are

$$\boldsymbol{\xi}_i(t) = \int_{\partial C_i \cap \partial \Omega} \mathbf{n} \quad \text{and} \quad \nu_i(t) = \int_{\partial C_i \cap \partial \Omega} \mathbf{v} \cdot \mathbf{n}, \quad (6)$$

and \mathbf{u}_∂ is the value of the solution which satisfies the boundary conditions [12].

In the presented computations the numerical flux function of equation (3) is replaced by a Total Variation Diminishing (TVD) numerical flux [13, 6]. To this purpose, a flux limiter approach has been followed and the second order centered approximation is replaced by the first order Roe flux near flow discontinuities [14]. The switch is controlled by the limiter proposed by van Leer [13]. The above high-resolution version of the scheme requires the definition of an extended edge data structure that includes also the extension nodes i^* and k^* , that are needed in the evaluation of the limiter function. As done by Ref. [15], the extension nodes belong to the two edges best aligned with $i-k$.

When dealing with moving/deforming meshes in the ALE framework an additional constrain is usually enforced to prevent spurious oscillations to appear in the solution. Such constrain is expressed as a conservation equation for the cell volumes termed Geometric Conservation Law (GCL) that can be automatically satisfied if the integrated velocities are computed as the derivatives of the volumes swept by the corresponding interfaces, i.e.

$$\nu_{ik}(t) = \frac{dV_{ik}}{dt} \quad \text{and} \quad \nu_i(t) = \frac{dV_{i,\partial}}{dt}. \quad (7)$$

where V_{ik} is the volume swept by the interface ∂C_{ik} and where $V_{i,\partial}$ is the volume swept by the interface $\partial C_i \cap \partial \Omega$.

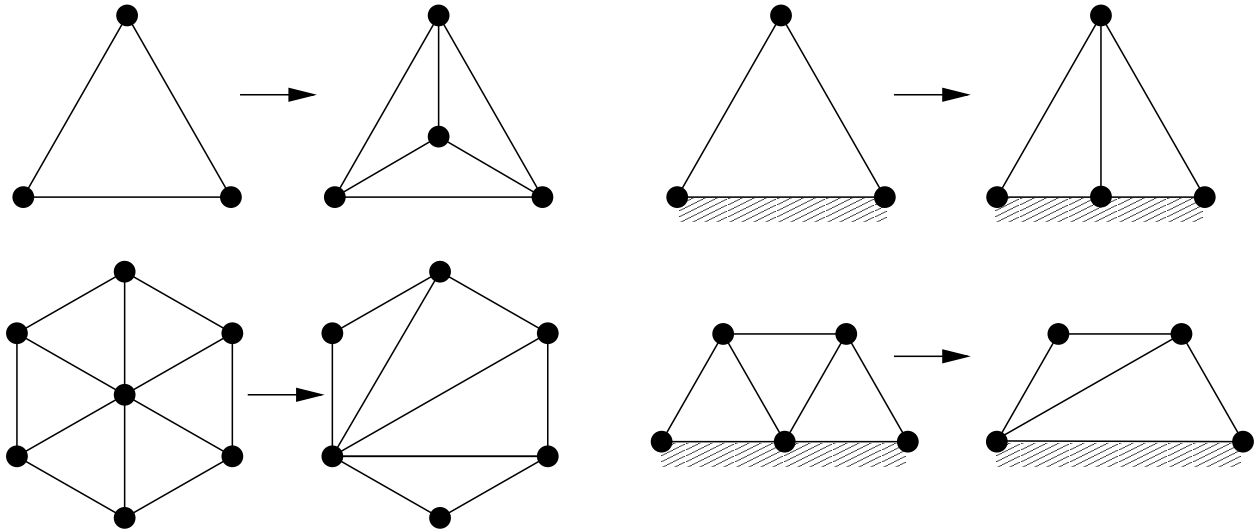


Figure 3: Top: refinement pattern by node insertion in the center of mass of an existing element for a domain (top-left) element and boundary (top-right) element. Bottom: Derefinement pattern by node deletion for a domain (bottom-left) element and boundary (bottom-right) element.

A more general version of equation (2) for adaptive grids is given by

$$\left\{ \begin{array}{l} \frac{d}{dt}[V_i \mathbf{u}_i] = \sum_{k \in \mathcal{K}_{i, \neq}(t)} \Phi(\mathbf{u}_i, \mathbf{u}_k, \nu_{ik}, \boldsymbol{\eta}_{ik}) + \Phi^\partial(\mathbf{u}_i, \nu_i, \boldsymbol{\xi}_i), \\ \frac{dV_{i, ik}}{dt} = \nu_{ik}, \\ \frac{dV_{i, \partial}}{dt} = \nu_i, \end{array} \right. \quad \begin{array}{l} \forall i \in \mathcal{K}(t) \\ \forall k \in \mathcal{K}_{i, \neq}(t) \end{array} \quad (8)$$

where both the number of nodes, \mathcal{K} , and the connectivity, $\mathcal{K}_{i, \neq}$, may vary during the the computations. The ODE system above is solved using a Backward Differences Formulæ (BDF) scheme of order either one or two, as reported in the numerical results section. At each time level, a dual time-stepping technique is used to solve the non linear system of equations for the vector unknown at time $n + 1$ [16].

The numerical scheme outline above is used together with mesh adaptation techniques. The local changes in grid topology, e.g. edge-swapping and node insertion/deletion, are interpreted as a continuous deformation of the finite volumes associated to the grid. As an example, in fig. 2 the geometrical interpretation of edge-swapping in a continuous framework is sketched. The interface velocities given of equation (7) are thus computed taking into account the distortion of the finite volumes caused by such modifications. The solution onto the new, adapted, grid can therefore be computed simply integrating Eq. (8) without any explicit interpolation step. Additional flux contributions must be taken into account for every removed edge [8, 17] and additional conservation equations must be integrated for every removed node [7] in order to ensure the conservativity of the resulting scheme. Such additional fluxes and equations can be dropped after a given number of time steps depending on the time-integration scheme adopted, e.g. two for a BDF2 and three a BDF3, since their contribution is identically equal to zero. The reader is referred to [8, 18, 7] for a detailed description of the ALE interpretation of grid adaptation.

2 Grid Alteration Strategy

In the present work, mesh adaptation strategies are used to locally modify the grid spacing so that the numerical error is evenly distributed within the elements of the computational domain and so that the size of the element is not greater than a given size distribution which is proportional to the distance from the

boundaries. Mesh adaptation is performed by applying a suitable mixture of global and local techniques: nodes displacement via elastic analogy, edge swapping, node insertion and removal, as shown in figure 3.

Based on the geometry of the grid, an element i is be refined if $h_i > \mathcal{A}(\mathbf{x}_i)$, where h_i is the size of the element and $\mathcal{A}(\mathbf{x})$ is a known function that prescribed the maximum size of the elements inside the domain. Since in most cases of aerodynamic interest it is desirable to generate highly refined zones close to solid bodies, in the present work it has been chosen to impose the dimension of the grid with a linear law, proportional to the distance from boundaries.

According to the principle of error equidistribution, nodes will be inserted in the regions where the error is greater than the domain average, or deleted where it is smaller. A triangular element is marked for refinement if the error is larger than a given threshold, e.g.

$$\frac{1}{3} \sum_i \mu(E_i(M)) + 0.1\sigma(E_i(M)),$$

where the sum is performed amongst the element nodes, E_i is the elemental error, μ is the domain average of the error and σ is the standard deviation. Conversely, the grid-coarsening threshold is set equal to $0.98\mu(E(s))$, to force grid adaptation towards a greater uniformity in error distribution. The adopted elements refinement and nodes removal techniques are shown in fig. 3.

Since the exact value of the error is obviously unknown, the numerical error E has to be locally estimated. In most applications, error estimators are either functions of gradient or undivided differences [19, 20, 21, 22], or functions of the Hessian matrix \mathcal{H} [23, 24, 22, 25, 26] of a convenient sensor variable which is representative of the flow features and whose choice depends on the physical problem. In the present study, to cope with the presence of shock waves and smooth-flow regions, the following Mach based nodal estimator is used

$$E_i = h_i^2 \sqrt{E_i^2(\mathbf{m}_\tau, M) + E_i^2(\mathbf{m}_n, M)},$$

with

$$E_i(\mathbf{m}, M) = \frac{\mathbf{m}^T \mathcal{H}(M) \mathbf{m}}{h_i \mathbf{m}^T \nabla M + 0.12 \mu(M)} + \frac{\mathbf{m}^T \nabla M}{h_i^3 \mathbf{m}^T \nabla M + 0.12 \mu(M) h_i}, \quad (9)$$

where h_i is longest edge of the i -th element M is the Mach number and \mathbf{m}_τ and \mathbf{m}_n are the tangential and normal components of the linear momentum vector respectively. The discrete Hessian matrix and the gradient vector are computed using a finite-element approximation within the node-pair representation [27, 28]. Equation (9) is a modification of the error estimator proposed by Webster [26].

In order to improve the grid quality, standard edge-swapping and grid smoothing techniques are also adopted [29].

In order to perform unsteady computations with adaptive grids the following predictor-corrector method is used. At a given time level t_n a prediction of the solution is computed from the known values of the solution. The grid adaptation procedure is then carried out, based on the error estimated with computed prediction. A higher-order solution is then calculated at the time t_{n+1} over the new adapted grid.

3 Free vortex advection

The case of the advection of a vortex in an horizontal flow is presented. A two dimensional vortex is represented by the Bagai-Lieshman compressible vortex [30]. The so called $n = 1$ Scully [31] model is used for the velocity field, namely

$$\frac{m_\theta(\hat{r})}{\rho(\hat{r})} = \frac{2\hat{r}}{(1+\hat{r}^2)} M_c c_\infty, \quad (10)$$

where $\hat{r} = |\mathbf{x}|/r_c$, r_c is the vortex core radius, M_c is a reference value for the vortex core Mach number and c_∞ is the value the speed of sound for \hat{r} that goes to infinity. As it is commonly done in the literature the vortex core Mach number can be expressed in terms of the vortex intensity Γ_c and radius r_c , namely $M_c = \Gamma_c / (4\pi r_c c_\infty)$.

Following Bagai and Lieshman [30], the density and pressure field are computed from the radial momentum component of the compressible Navier-Stokes equations for an isentropic flow and an ideal gas,

namely

$$\rho(\hat{r}) = \rho_\infty \left(1 - 2 \frac{\gamma - 1}{1 + \hat{r}^2} M_c^2 \right)^{\frac{1}{\gamma-1}} \quad \text{and} \quad P(\hat{r}) = \frac{c_\infty^2 \rho_\infty}{\gamma} \left(\frac{\rho(\hat{r})}{\rho_\infty} \right)^\gamma \quad (11)$$

where ρ_∞ is the density value far away from the vortex.

The compressible vortex defined above is then inserted in a uniform horizontal flow which is completely defined by the Mach number M_∞ , the density ρ_∞ and the momentum modulus m_∞ . Indeed, the non-dimensional speed of sound of Eq. (10) is therefore given by $c_\infty = \frac{m_\infty}{M_\infty \rho_\infty}$. In the present work a unit value has been chosen for both the free-flow density and momentum, thus only the free-flow and vortex Mach number are used to completely define the flow field.

3.1 Fixed grid computations

The finite-volume scheme is first tested over the compressible vortex advection case. The free flow Mach number is 0.8, the vortex Mach number is 0.2 and $r_c = 0.1$ grid units. The lower half of the fixed computational grid is shown in fig. 4 together with the upper half of the density contour lines. The grid dimensions are $240 r_c \times 120 r_c$ and it is made of 61015 nodes and 121722 elements. Non reflection boundary conditions are imposed on every side of the rectangular domain, where the far field state u_∞ is taken as the exact solution to the problem, i.e. the rigid displacement of the vortex along the horizontal axis with velocity $M_\infty c_\infty$.

To test the time-convergence properties of the scheme unsteady computations have been carried out for different values of the Courant number and with different time schemes, i.e. BDF scheme of order 1, 2 and 3. The global Courant number is computed as $Co = \frac{m_\infty \Delta t}{\rho_\infty h_{min}}$, where $h_{min} = 0.005$ is the smallest edge of the grid, and ranges between 0.1 and 20. The computations are interrupted when the vortex has been displaced of 100 core radius, i.e. $t = 10$.

In fig. 5 the final solution obtained adopting different schemes and time-steps is plotted in terms of tangential component of the velocity computed along the symmetry plane, i.e. $y = 0$. For values of the Courant number lower than 1 the numerical error introduced by the time scheme is very small, indeed the curves obtained with the three schemes are overlapped and difference with respect to the exact solution is given by the error in space. Increasing the Courant number to 1 highlights the differences between the first order scheme and the more accurate ones. In the $Co = 20$ case, shown in fig. 5(c), the difference between the exact solution and the numerical one is increased and the behavior of the three schemes differs. The curve obtained with the first order BDF is strongly smeared but still monotone. The solution obtained with the second order scheme is less dissipated but shows an error in phase that is not present in the other cases. The curve computed with the third-order scheme shows a similar delay in phase but, differently from the BDF2 scheme, does not show a monotone behavior. This result is in agreement with the fact that the high-order (in time) extension of first order TVD scheme does not necessarily share the total variation diminishing property. Indeed Fernandez [32] showed that in the 1D Sod problem the implicit BDF2-Roe scheme is not monotone for $Co = 5$, while Ruuth et al. [33, 34] set a maximum Courant to ensure monotonicity of a BDF2 scheme in the one-dimensional case at 0.5 times the maximum Courant of the corresponding first-order explicit scheme.

In fig. 6 the iso-vorticity lines at $t = 10$ are shown for the exact solution, while the one obtained with the tested numerical schemes are presented in fig. 7. The number of contour lines and the spacing is the same adopted in fig. 6.

For $Co = 0.1$ the numerical solutions are almost distinguishable amongst each other, while for $Co = 1$ only the vorticity computed with the first order BDF appear to be smeared and the effects of the entropy fix are visible, i.e. the different amount of introduced numerical dissipation between the upper and the lower side of the vortex also causes an error in phase. For $Co = 20$ the solution obtained with the first order scheme is almost completely dissipated, while the one obtained with the high-order schemes features an error in both phase and amplitude. The non-monotone behavior of the scheme that has been shown in fig. 5(c) is here not visible due to the close-up view, but it is nonetheless present in the vorticity as well.

Therefore to ensure the monotonicity of the solution the first-order Forward Euler scheme is adopted, indeed the bound in terms of Courant number is such that the error introduced by the first order and the high-order schemes is comparable, as shown in fig. 5(a) and 7(a).

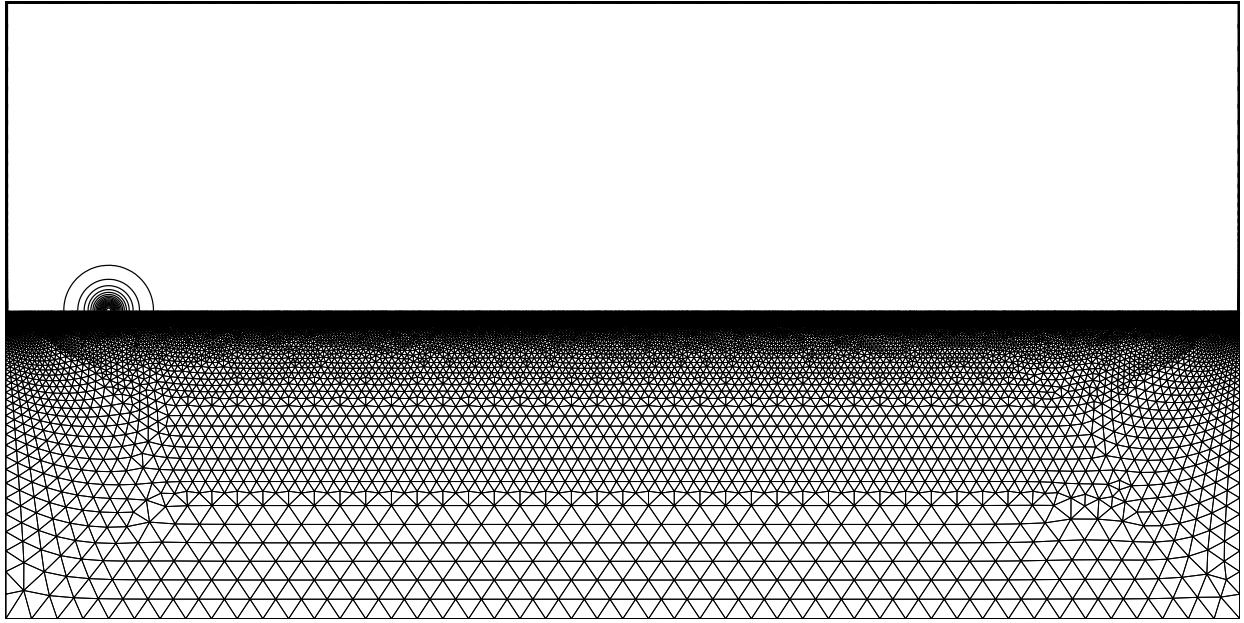


Figure 4: Lower half of the fixed mesh and upper half of the initial density contour lines. The size of the mesh is $240 r_c \times 120 r_c$, with 61015 nodes and 121722 elements. The minimum node spacing is roughly of 0.005 grid units.

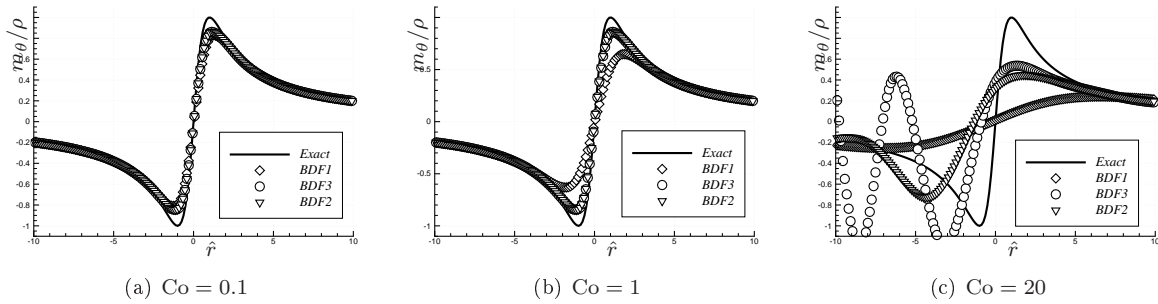


Figure 5: Tangential component of the velocity along the symmetry line as a function of the radial coordinate at the non-dimensional time $t = 10$. The vortex displacement is equal to $100 r_c$.

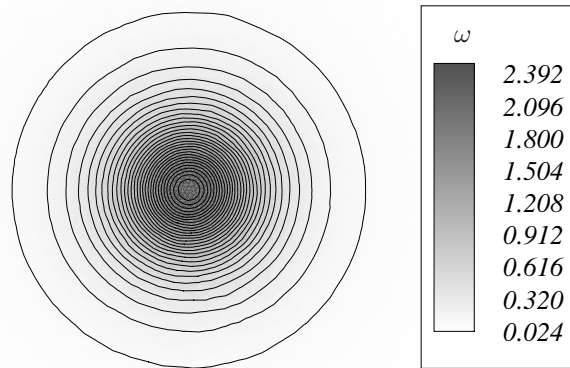


Figure 6: Contour lines of the magnitude of the vorticity vector of the initial solution.

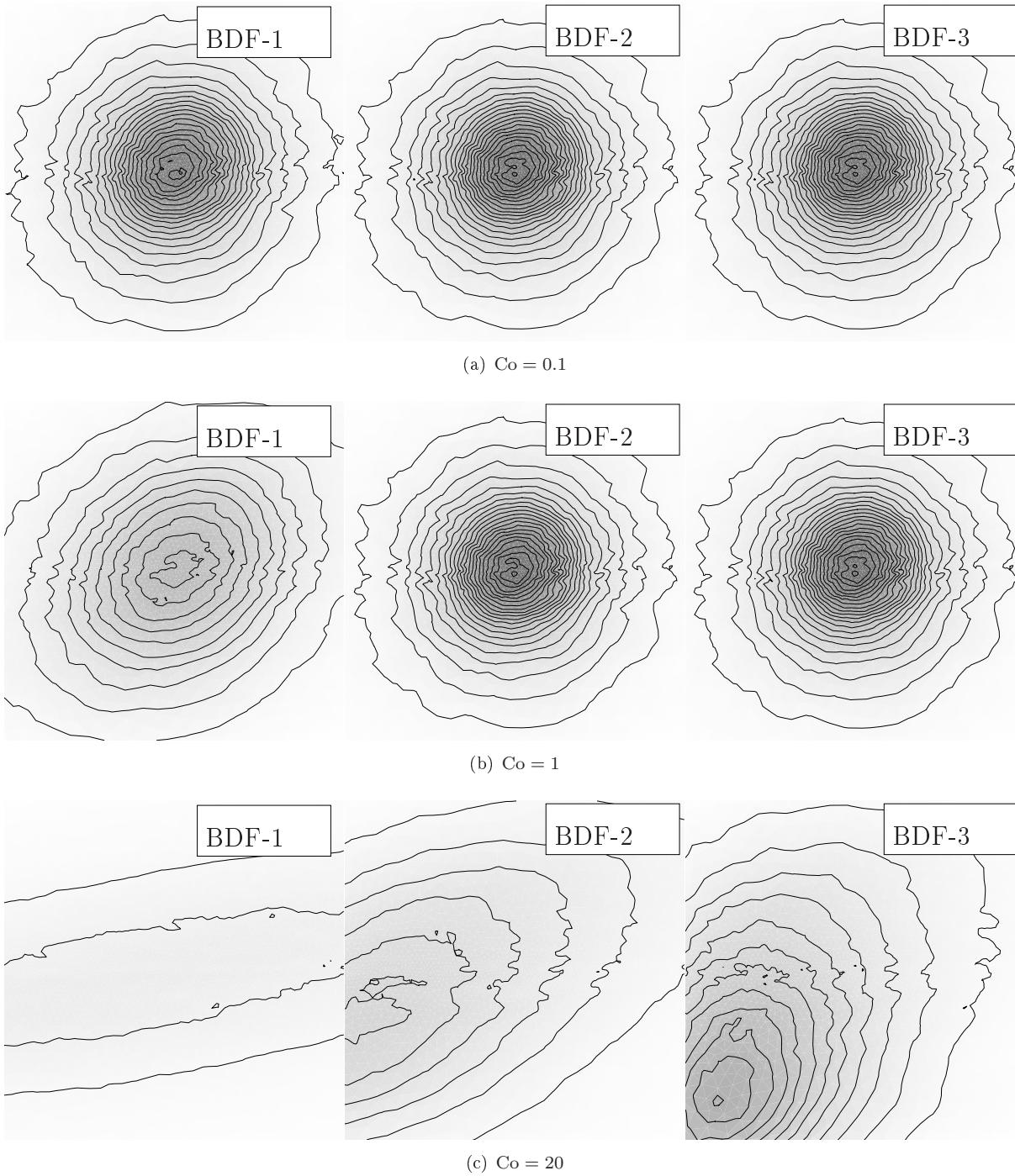


Figure 7: Contour lines of the magnitude of the vorticity vector obtained at $t = 10$ with different time-steps and numerical schemes. The number of contour lines and the scale is the same adopted in fig. 6

Test Case	Adapted	Rigid	Rigid Adapted	Baeder 8 th order	Baeder 5 th order	Kwon
$\frac{\Delta v_v(T)}{\Delta v_v(0)} - 1$	-0.58	-0.051	-0.05	+0.032	-0.15	-0.02

Table 1: Variation of the velocity on the edge of the vortex core with respect to the initial value for the vortex advection problem.

3.2 Adaptive grid computations

As shown in the previous section the artificial dissipation introduced by the scheme is responsible of the destruction of the vortex core. This can be avoided reducing the time step and the local grid spacing. To this hand the grid adaptation tools described in section 2 are here applied to the vortex transport problem.

The free-flow Mach number is 0.8, vortex core Mach number is 0.255 and vortex radius is 0.05. The initial grid and the vorticity field are shown in fig. 8. The grid is $480 r_v \times 80 r_v$ and is made of 33017 nodes and 65368 elements. Away from the vortex the grid spacing is 0.08, i.e. $h_{max} = 5.5 \times 10^{-2}$, and around the vortex core a refined region is created with elements of area 3×10^{-3} , i.e. $h_{min} = 0.002$. The geometry-driven adaptation outlined in section 2 is used to generate a constant area region inside a circumference of radius $2r_v$ centered on the vortex core. Moreover the element size decreases linearly and at $r \simeq 4r_v$ the maximum area is recovered, as shown in fig. 8(d).

The contour lines for the magnitude of the vorticity vector are shown in fig. 8(c). Although the prescribed solution of Eq. (10) is smooth, the vorticity is slightly non monotone possibly due to the effect of the variable grid spacing.

Following [5], in the unsteady computations the position of the vortex core \mathbf{x}_v^{n+1} is taken as the grid vertex featuring the minimum/maximum of ω within the circle of radius $0.5 r_v$ centered in \mathbf{x}_v^n . Following [35] to measure how well the initial solution is preserved the variation of the velocity along the vortex radius is introduced, i.e.

$$\Delta v_v(t) = \max_{i \in \mathcal{K}(t)} \left| \frac{\mathbf{m}_i(t)}{\rho_i(t)} - \frac{\mathbf{m}_\infty}{\rho_\infty} \right| - \min_{i \in \mathcal{K}(t)} \left| \frac{\mathbf{m}_i(t)}{\rho_i(t)} - \frac{\mathbf{m}_\infty}{\rho_\infty} \right|.$$

At a given time the error indicator is thus taken as $\Delta v_v(t)/\Delta v_v(0) - 1$.

The adaptation procedure is carried out to adapt the solution over a sensor made by the sum of the magnitude of vorticity and the magnitude of the gradient of ρ and to satisfy the geometric constraints sketched above, i.e. the element size decreases linearly with the distance from the vortex core but the extrema are bounded by the smallest and the largest elements present in the the initial mesh, i.e.

$$\mathcal{A}(\mathbf{x}_i, t) = (h_{max} - h_{min})\mathcal{A}_v(\mathbf{x}_i, t) + h_{min}, \quad (12)$$

where

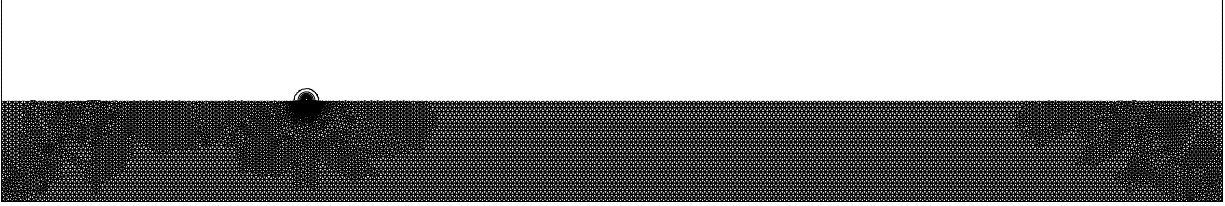
$$\mathcal{A}_v(\mathbf{x}, t) = \frac{1}{3} \min \left(\max \left(\frac{|\mathbf{x} - \mathbf{x}_v(t)|}{r_v}, 3 \right), 0 \right)$$

is the normalized distance from the core and h_{min} and h_{max} are the minimum and maximum element size of the domain, respectively.

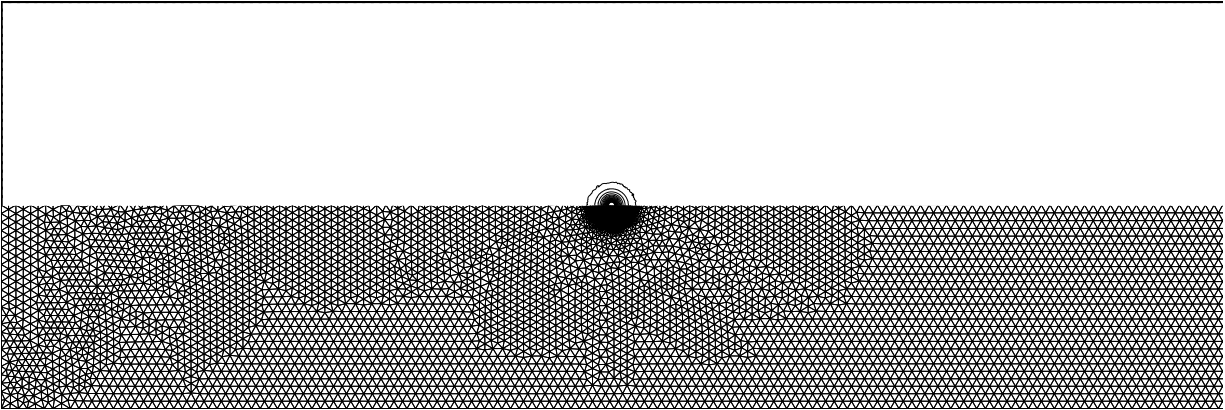
The computations are carried out with a non-dimensional time step of 5×10^{-4} , which correspond to a Courant number of 0.1, and are interrupted at $t = 4$, i.e. when the total distance traveled by the vortex core is $80r_v$. The final solution and grid are plotted in fig. 9. The overall grid-quality is unsatisfactory and this is indeed reflected over the iso-vorticity lines of fig. 9, which appear to be excessively irregular. Overall the solution obtained adapting over ω and $\nabla \rho$ is severely smeared resulting in a 58% error, as shown in tab. 1. This result is unsatisfactory if compared to other adaptive mesh approaches to the vortex advection problem [5, 35].

As shown in fig. 9 the applied adaptive scheme is strongly dissipative. The numerical dissipation introduced by the TVD Roe scheme is proportional to the eigenvalues of the Jacobian matrix, i.e. \mathbf{m}/ρ , c and ν , and to the cell size, i.e. η .

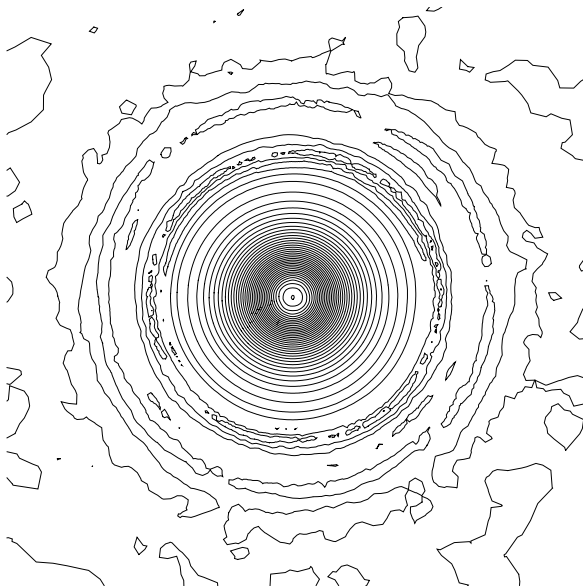
The grid velocity terms is both proportional to the fixed-topology grid displacement, i.e. the displacement



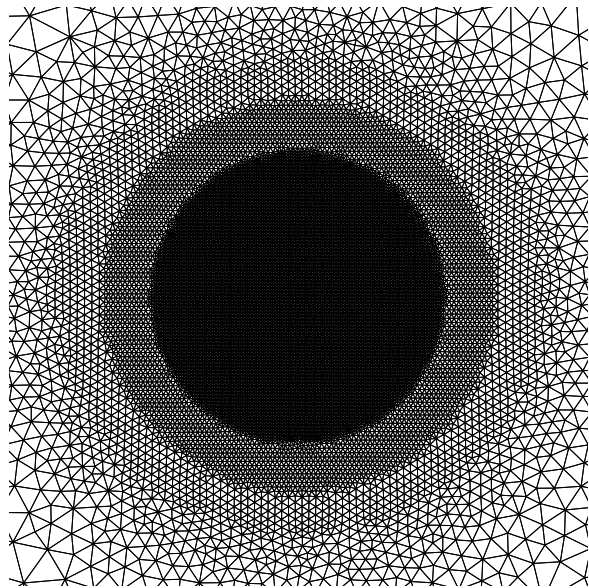
(a) Initial grid and vorticity contour



(b) Left half of the initial with vorticity contour



(c) Vorticity contour close-up



(d) Initial grid close-up

Figure 8: Initial grid and solution vorticity magnitude for the vortex advection problem with adaptive the scheme. Grid made of 33017 nodes and 65368 elements, $h_{max} = 0.08$ and $h_{min} = 0.002$, with $h_{max} = 5.5 \times 10^{-2}$ and $h_{min} = 1.36 \times 10^{-3}$.

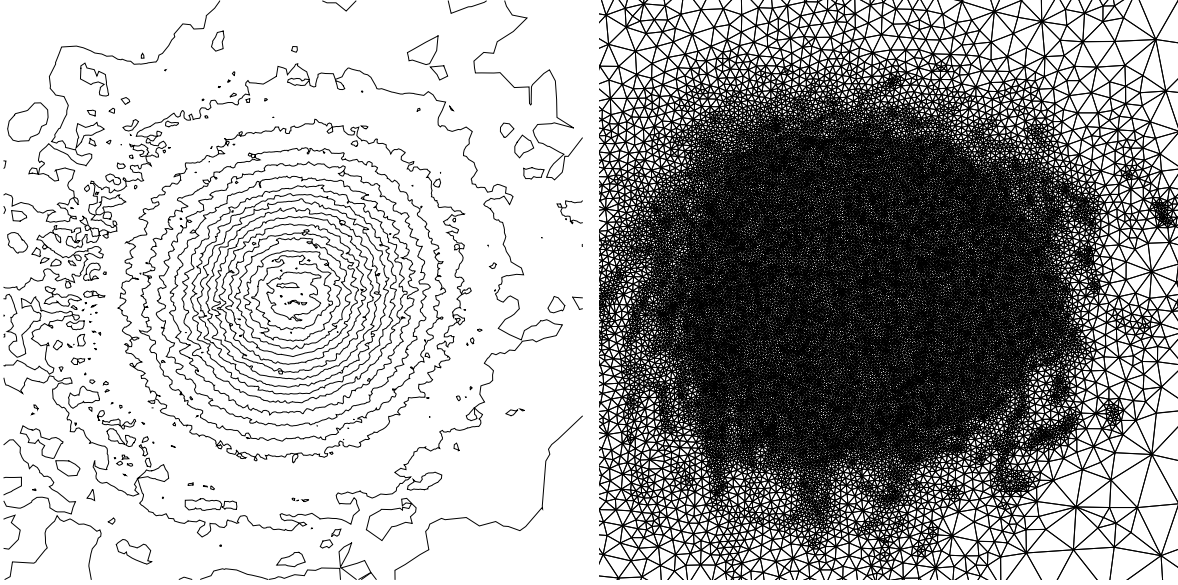


Figure 9: Final grid and solution vorticity magnitude for the vortex advection problem with adaptive the scheme and no mesh deformation, 40687 nodes and 80623 elements.

of the refined area around the vortex, and to the correction term to account for the insertion/deletion of nodes. The latter term depends inversely on the time step [36]. From the governing equations point of view this means that the more the time step is reduced, and the more frequently the grid is changed, the more numerical dissipation will be introduced by the scheme.

In the adaptation case of fig. 9 the grid around core is continuously changing due to the effect of the vortex displacement and of the solution smearing as well. To overcome such issue a different approach has been studied that limits the amount of topology modifications performed to move the vortex core. The mesh deformation algorithm is modified to displace in rigid-like fashion the elements around the vortex core, \mathbf{x}_v , and a predictor/corrector-like scheme is set up as follows

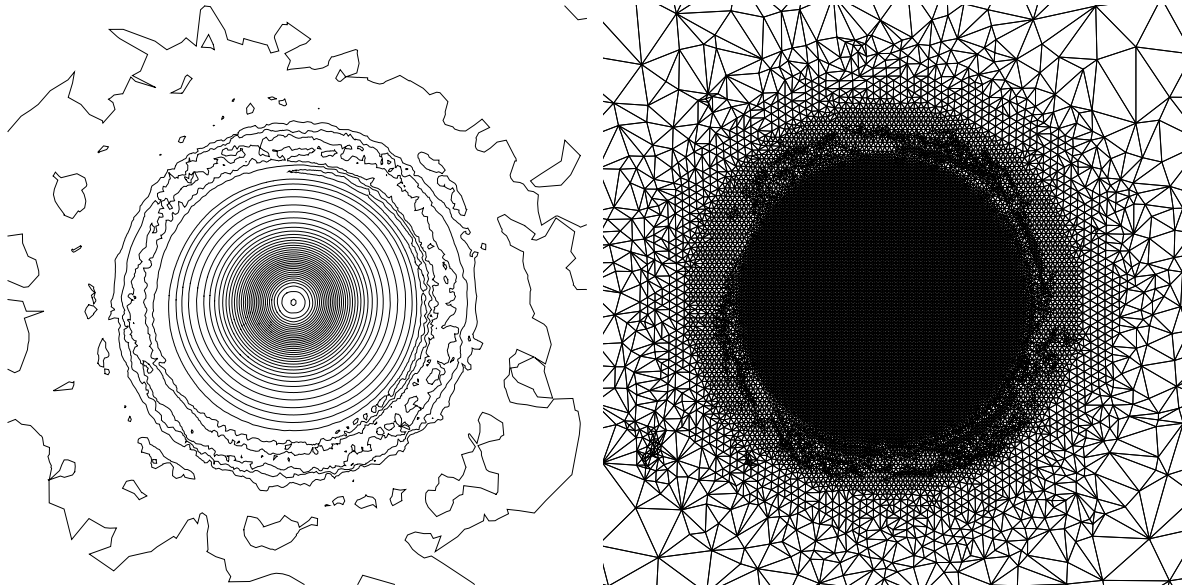
1. First the position of the vertex representing the vortex center point at the new time step is predicted as

$$\hat{\mathbf{x}}_v^{n+1} = \mathbf{x}_v^n + \frac{\Delta t}{2} \left(\frac{\mathbf{m}_v^n}{\rho_v^n} + \frac{\mathbf{x}_v^n - \mathbf{x}_v^{n-1}}{\Delta t} \right),$$

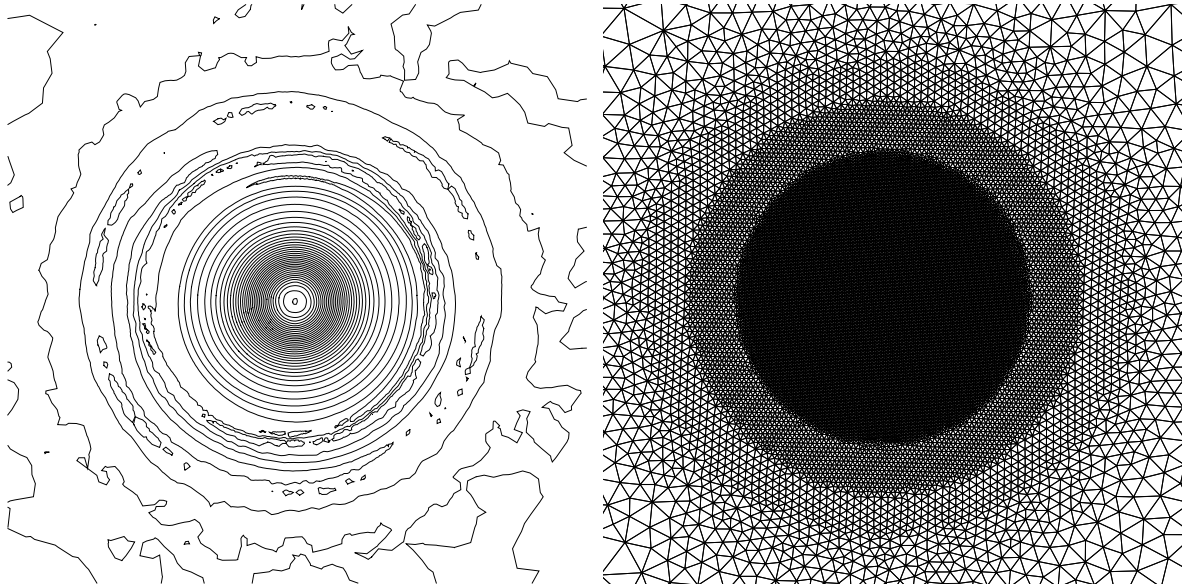
where \mathbf{m}_v and ρ_v are the values of momentum and density on the core node, respectively.

2. The position of the rest of the grid nodes \mathbf{x}_i^{n+1} is computed with the mesh deformation scheme based on the continuum analogy. The elements located in side the vortex core are displaced rigidly of $\hat{\mathbf{x}}_v^{n+1} - \mathbf{x}_v^n$, the elements located outside the mesh are deformed with the elastic analogy algorithm.
3. Following the FIAP procedure, the solution at the new time step is predicted and then the position \mathbf{x}_v^{n+1} is updated locating the minimum/maximum of the vorticity, as sketched above. In the present case the application of the mesh regularization technique is not applied inside the vortex core, since it would a negative impact on the grid spacing, thus on the solution.
4. The de/refinement scheme outlined in section 2 is carried out based on the corrected position for the vortex core and the predicted solution the grid. This allows to impose simultaneously the constraints based on the error equidistribution theory and the geometric ones.
5. The solution u^{n+1} is updated with the ALE scheme over the adapted grid.

The solution computed with the scheme outlined above are shown in fig. 10(a). The initial grid quality and spacing are very well preserved, and the vorticity field is very close to the exact one, indeed, as shown in



(a) Adaptive, 36999 nodes and 73198 elements



(b) No-adaptation, 33017 nodes and 65368 elements.

Figure 10: Final grid and solution vorticity magnitude for the vortex advection problem with the adaptive scheme. (a) Mesh deformation and FIAP adaptation with geometric constraints on the element dimension. (b) Mesh deformation and swapping only.

tab. 1 a 5% loss is achieved that is comparable with the 8-th order scheme from [35]. A similar result can be obtained if no nodes are inserted or deleted and the movement is carried out only with mesh deformation and swapping, as shown in fig. 10(b). Indeed, since the grid inside the vortex core is translated almost rigidly, no changes in topology occurs inside this region and the vortex is thus translating “together” with a high quality/resolutions mesh.

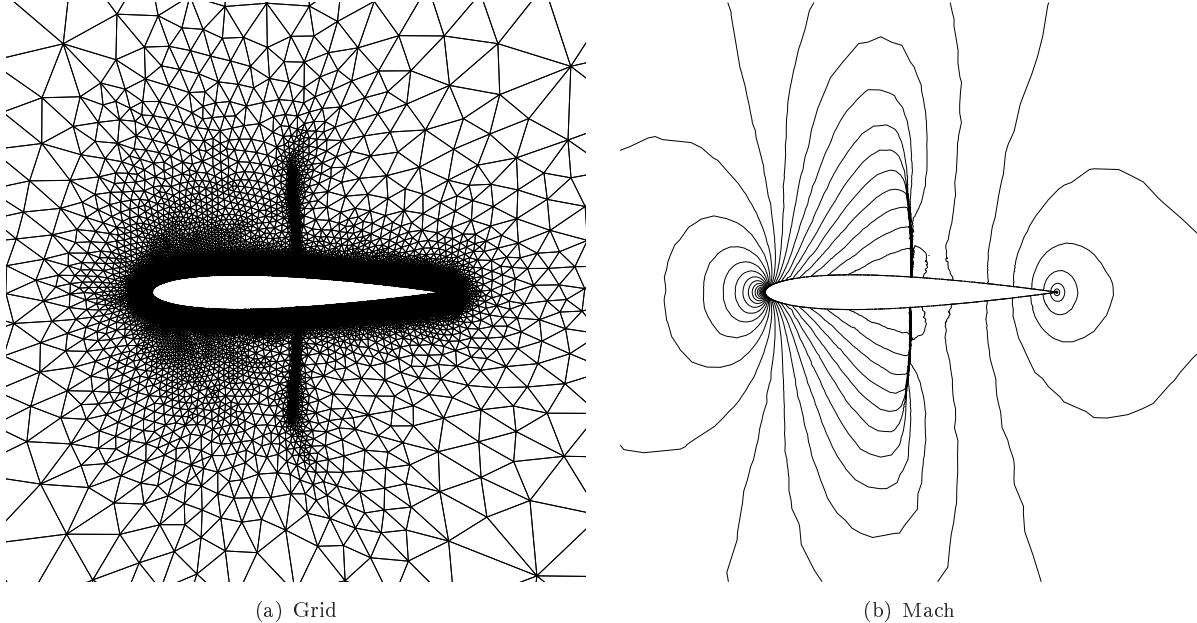


Figure 11: Initial adapted grid and solution for a $M_\infty = 0.8$ flow past a NACA 0012 at zero angle of attack. Initial grid is made of 50867 nodes and 100595 elements, i.e. $h_{min} = 6.4 \times 10^{-4}$ and $h_{max} = 1$.

x_v/c	-0.6	-0.2	0.2	0.6	1.0	1.4
$\frac{\Delta v_v(t)}{\Delta v_v(0)} - 1$	0.1333	-0.1084	-0.3791	-0.3857	-0.4621	-0.5097

Table 2: Reduction in vortex intensity measured in terms of tangential velocity across the vortex core.

4 Interaction with a NACA 0012 airfoil

The interaction between a NACA 0012 airfoil and a vortex is here presented. The flow field Mach number is 0.8 and the vortex reference Mach number is 0.259154, which correspond to $\Gamma = -0.2$, i.e. rotating clockwise. The airfoil has a unit chord value, i.e. $c = 1$, and the vortex core has a $0.05c$ radius and the initial position is $x_v(0) = -5c$ and $y_v(0) = -0.26c$.

As shown by [37, 38, 5], when the distance between the vortex and the lower side of airfoil is sufficiently small an increase in the value of the local velocity on the wall is observed, while the flow field on the upper side is only slightly affected. This causes a pressure wave to be released by the nose of the airfoil, that propagates upstream, and a aft movement of the shock wave on the lower side due to the increase in streamwise velocity. When the vortex reaches the trailing edge the shock wave on the lower side moves fore, due to the reduction of the jump of velocity/pressure, and as the time proceeds the original, steady, state is recovered.

First steady computations are carried out with adopting the FIAP adaptive scheme for the NACA 0012 airfoil test case at zero angle of attack without vortex. The solution features two strong shocks on the upper and lower side of the airfoil with equal intensity, indeed no shear surface is present.

The FIAP scheme for steady applications is adopted, i.e. without looping over s , to adapt the solution to the mixed Gradient/Hessian of the Mach number until a 5% convergence is obtained for the relative variation of μ_w . The distance-based adaptation of section 2 is also carried out imposing that the size of the elements decreases with the distance from the airfoil and with the distance from the vortex located in $\mathbf{x}_v(0)$, i.e. evaluating Eq. (12) with $h_{max} = 1$ and $h_{min} = 6.4 \times 10^{-4}$. Therefore the area of the elements located inside the core is one order of magnitude smaller than the elements located on the boundary of the airfoil.

The obtained grid is shown in fig. 11(a) which is made of 50867 nodes and 100595 elements. The simultaneous use of the solution-based and the geometry-based adaptation strategies allows to obtain a grid that is very well refined near close to the shocks and, on the other hand, is not under refined where the error

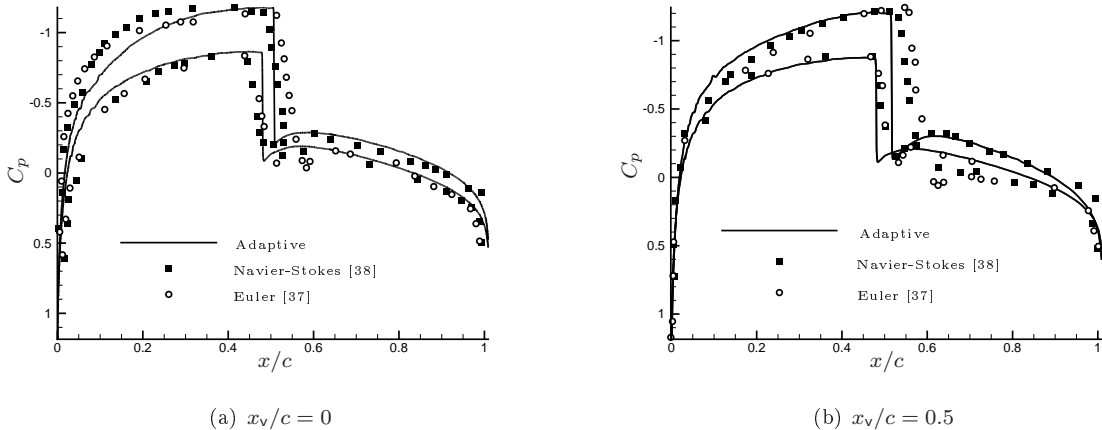


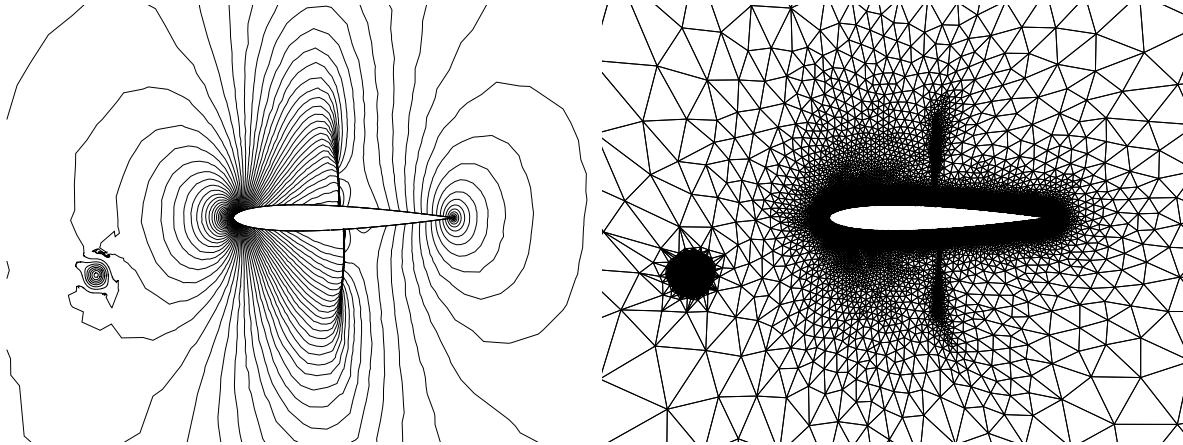
Figure 12: Comparison between the pressure coefficient computed with the adaptive scheme for the Parallel BVI problem and the Euler [37] and Navier-Stokes [38] reference solutions.

sensor is small. Indeed the grid obtained with the solution-driven scheme only feature very large elements in the region between the nose of the airfoil and the shock wave, the use of the geometry-driven scheme avoid such behavior. This “conservative” approach, which limits the grid derefinement, is considered a better choice when performing unsteady computations during which the mesh undergoes significant modifications. In fig. 11(b) the contour lines for the Mach number are shown: the solution is overall symmetric, the shock wave are very well resolved and no shear wake is present.

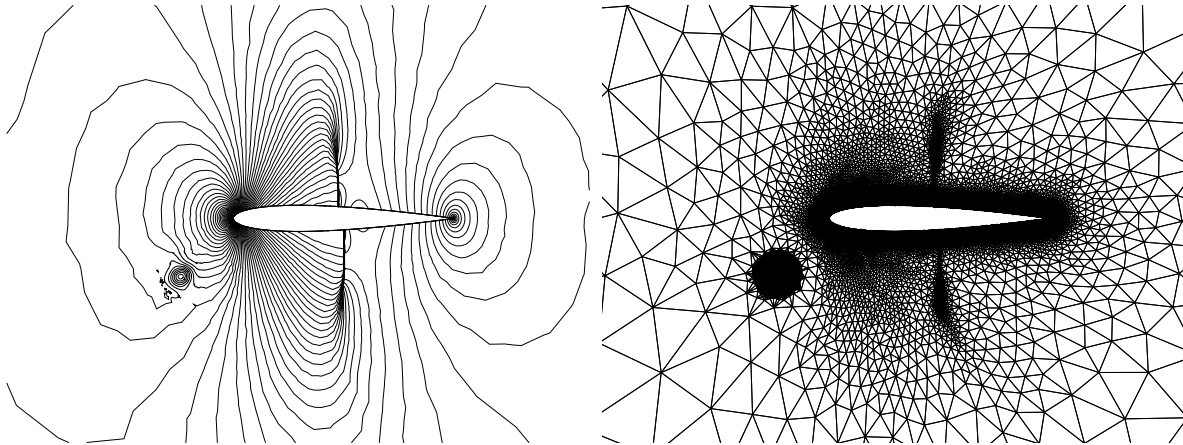
To perform unsteady computations where the vortex travels very close to the airfoil, i.e. with very a small miss-distance, a vortex is “inserted” in the flow field. To this purpose the initial solution is calculated superimposing the solution obtained with the adaptive steady computations, i.e. the one of fig. 11, and the solution computed evaluating Eq. (10) and (11) for the vortex with described above. The FIAP scheme is then carried out without looping over s , i.e. performing one adaptation procedure per time instant, using a Forward Euler scheme with a non dimensional time-step of 0.08, corresponding to a maximum Courant number of 80.

The computational grid is shown in fig. 13 and 14 together with the pressure contour lines. The grid around the core follows closely the vortex, that is convected inside the domain and passes at small distance from the airfoil. The vortex, highlighted as a minimum in the pressure field, looses most of its intensity after the interaction with the airfoil with a 52% loss in terms of Δv_v when the core is located at $1.4c$, i.e. fig. 14(c). Fig. 13(b) and 13(c) shows that no pressure wave detaches from the leading edge as reported by [5], this could be caused by a reduction of the vortex intensity, as shown in tab. 2. The fore movement of the shock wave is also only mildly captured, to this end the reduction of almost 50% of the vortex intensity is a key factor together with the decrease of mesh quality that is caused by the close interaction of the vortex and the shock wave shown in fig. 14(a).

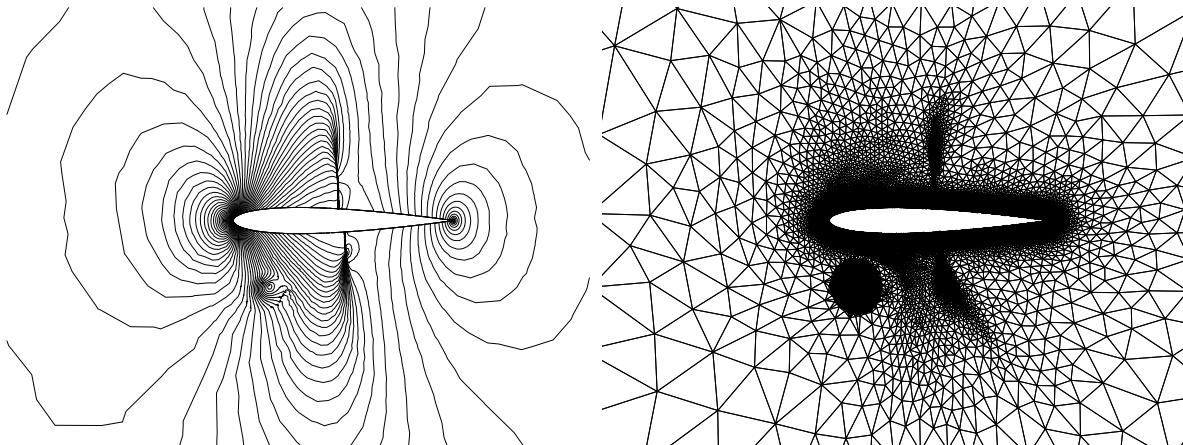
Fig. 12 shows the comparison between the distribution of the pressure coefficient along the airfoil computed with the adaptive scheme and the reference solutions obtained with an Euler solver [37] and a Navier-Stokes solver [38]. For $x_v = 0$ the curves on the upper side of the airfoil overlap fairly well, while the value of C_p on the lower side is higher than expected. This is in agreement with the fact that no compression wave is detached from the nose and could be caused by the reduction of the vortex intensity, as discussed above. The position of the lower-side shock and its intensity agree with the references. For $x_v = 0.5c$ the solution shows a better agreement in terms of pressure coefficient close to the nose, but the predicted aft movement of the upper shock is significantly underpredicted together with the increase in intensity. As before this is deemed to be caused by the strong reduction in the vortex intensity shown in tab. 2.



(a) $x_v/c = -0.6$, 48928 nodes and 96500 elements

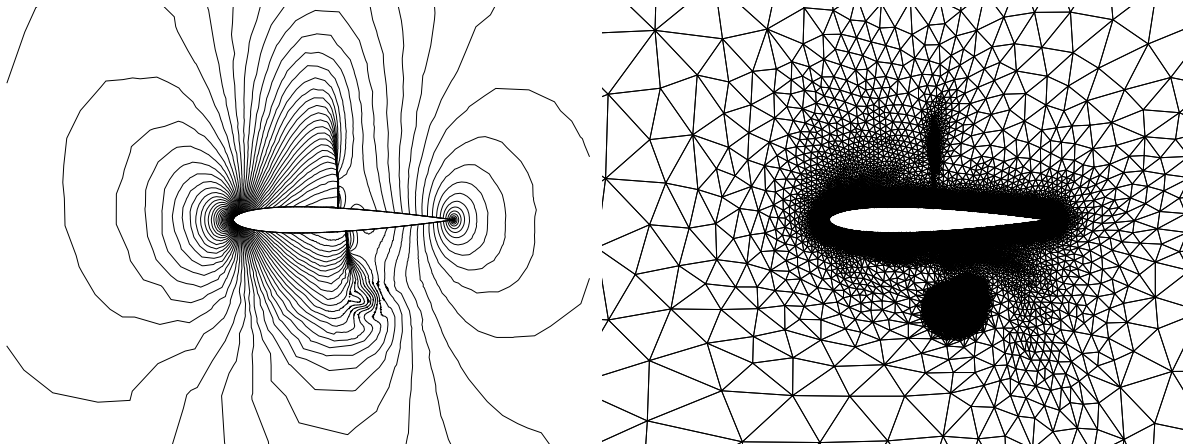


(b) $x_v/c = -0.2$, 48937 nodes and 96516 elements

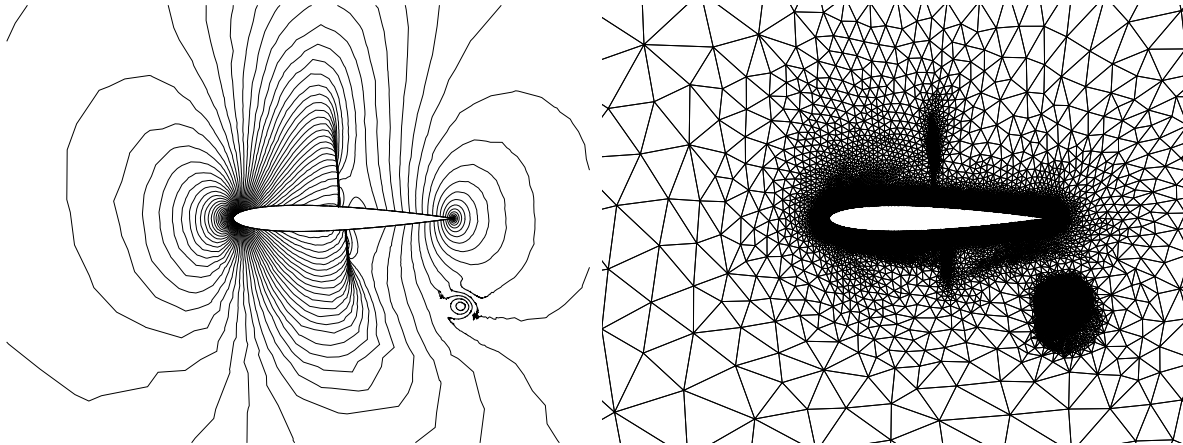


(c) $x_v/c = 0.2$, 48375 nodes and 95388 elements

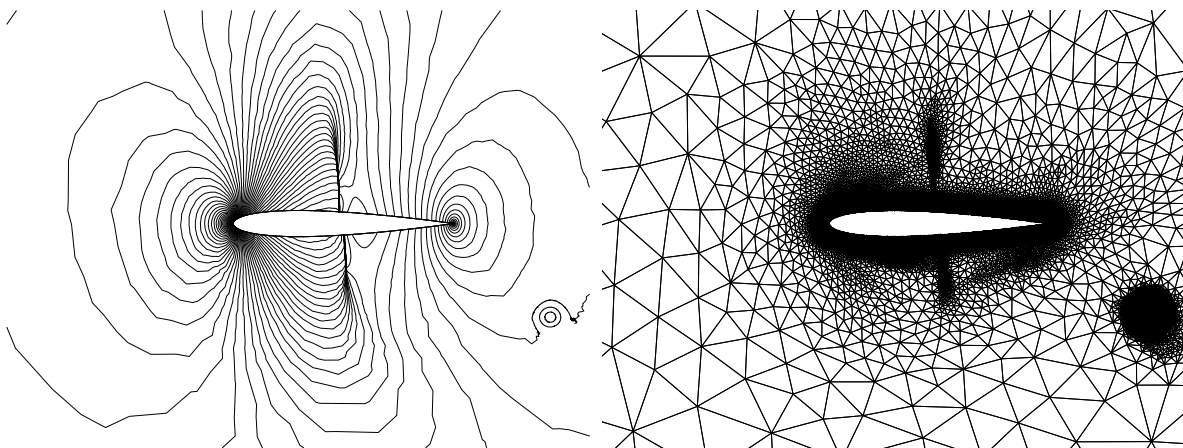
Figure 13: Computational grid and pressure contour for the parallel BVI NACA 0012 for $M_\infty = 0.8$, $M_v = 0.259154$ and $Co = 80$.



(a) $x_v/c = 0.6$, 48254 nodes and 95145 elements



(b) $x_v/c = 1$, 50565 nodes and 99761 elements



(c) $x_v/c = 1.4$, 50178 nodes and 98987 elements

Figure 14: Computational grid and pressure contour for the parallel BVI NACA 0012 for $M_\infty = 0.8$, $M_v = 0.259154$ and $Co = 80$.

References

- [1] R. Singh and J. D. Baeder. Adaptive euler simulation of supercritical interaction of airfoil and vortex. In *16th AIAA Computational Fluid Dynamics Conference, Orlando, FL, USA*, June 2003.
- [2] N. G. Hardin and S. M. Lamkin. Concepts for reduction of blade/vortex interaction noise. *J. Aircr.*, 24(2), 1987.
- [3] F. Malovrh and P. O. Gandhi. Sensitivity of helicopter blade-vortex-interaction noise and vibration to interaction parameters. *J. Aircr.*, 42(3), May–June 2005.
- [4] L. Tang and J. D. Baeder. On the significance of transonic effects on aerodynamics and acoustics of blade-vortex interactions. In *2nd AIAA/CEAS Aeroacoustics Conference*, 1996.
- [5] W.S. Oh, J.S. Kim, and O.J. Kwon. Numerical simulation of two-dimensional blade-vortex interactions using unstructured adaptive meshes. *AIAA J.*, 40(3):474–480, 2002.
- [6] R. J. LeVeque. *Finite volume methods for conservation laws and hyperbolic systems*. Cambridge University Press, 2002.
- [7] D. Isola, A. Guardone, and G. Quaranta. An ale scheme without interpolation for moving domain with adaptive grids. In *40th Fluid Dynamics Conference and Exhibit, AIAA*, 2010.
- [8] A. Guardone, D. Isola, and G. Quaranta. Arbitrary lagrangian eulerian formulation for two-dimensional flows using dynamic meshes with edge swapping. *J. Comput. Phys.*, 230(20):7706–7722, 2011.
- [9] J. Donea. An arbitrary Lagrangian-Eulerian finite element method for transient fluid–structure interactions. *Comp. Meth. Appl. Mech. Engng.*, 33:689–723, 1982.
- [10] J. Donea, A. Huerta, J.-Ph. Ponthot, and A. Rodríguez-Ferran. Arbitrary Lagrangian-Eulerian methods. In R. Stein, E. de Borst, and T.J.R. Hughes, editors, *The Encyclopedia of Computational Mechanics*, volume 1, chapter 14, pages 413–437. Wiley, 2004.
- [11] E. Godlewski and P. A. Raviart. *Numerical approximation of hyperbolic systems of conservation laws*. Springer-Verlag, New York, 1994.
- [12] A. Guardone and L. Quartapelle. Spatially factorized Galerkin and Taylor-Galerkin schemes for multi-dimensional conservation laws. Scientific Report DIA-SR 00-18, Politecnico di Milano, Italy, 2000.
- [13] B. van Leer. Towards the ultimate conservative difference scheme II. Monotonicity and conservation combined in a second order scheme. *J. Comput. Phys.*, 14:361–370, 1974.
- [14] P. L. Roe. Approximate Riemann solvers, parameter vectors, and difference schemes. *J. Comput. Phys.*, 43:357–372, 1981.
- [15] N. P. Weatherill, O. Hassan, M. Marchant, and D. Marcum. Adaptive inviscid solutions for aerospace geometries on efficiently generated unstructured tetrahedral meshes. In *AIAA Paper 93-3390-CP*. 11th AIAA Computational Fluid Dynamics Conference, Orlando, FL, 1993.
- [16] V. Venkatakrisnan and D. J. Mavriplis. Implicit method for the computation of unsteady flows on unstructured grids. *J. Comput. Phys.*, 127:380–397, 1996.
- [17] D. Muffo, G. Quaranta, and A. Guardone. Compressible fluid-flow ale formulation on changing topology meshes for aeroelastic simulations. In *Proceedings of the 26th ICAS Congress*, Anchorage, Alaska, September 14–19 2008.
- [18] D. Isola, A. Guardone, and G. Quaranta. Arbitrary lagrangian eulerian formulation for grids with variable topology. In *Proceedings of the III Int. Conf. on Computational Methods for Coupled Problems in Science and Engineering*. CIMNE, Barcelona, 2009.
- [19] T.J. Baker. Mesh adaptation strategies for problems in fluid dynamics. *Finite Elem. Anal. Des.*, 25:243–273, 1997.
- [20] R. Lohner. Mesh adaptation in fluid mechanics. *Eng. Fract. Mech.*, 50:819–847, 1995.
- [21] S. Pirzadeh. Unstructured viscous grid generation by the advancing layers method. *AIAA J.*, 32(8):1735–1737, 1994.
- [22] G. P. Warren, W. K. Anderson, J. T. Thomas, and S. L. Krist. Grid convergence for adaptive methods. In *AIAA 10th Computational Fluid Dynamics Conference*, 1991. AIAA Paper 91-1592.
- [23] M.J. Castro-Diaz, F. Hecht, B. Mohammad, and O. Pironneau. Anisotropic unstructured mesh adaptation for flow simulations. *Int. J. Numer. Meth. Fluids.*, 25:475–491, 1997.
- [24] J. Peraire, M. Vadhati, K. Morgan, and O.C. Zienkiewicz. Adaptive remeshing for compressible flow computations. *J. Comput. Phys.*, 72:449–466, 1987.
- [25] G. Xia, D. Li, and C. L. Merkle. Anisotropic grid adaptation on unstructured meshes. In *39th Aerospace*

- Sciences Meeting and Exhibit*, 2001. AIAA Paper 2001-0443.
- [26] B.E. Webster, M.S. Shepard, Z. Rhusak, and J.E. Flaherty. Automated adaptive time discontinuous finite element method for unsteady compressible airfoil. *AIAA J.*, 32:748–757, 1994.
 - [27] V. Selmin. The node-centred finite volume approach: bridge between finite differences and finite elements. *Comp. Meth. Appl. Mech. Engng.*, 102:107–138, 1993.
 - [28] M. Fossati, A. Guardone, and L. Vigevano. An edge-based mesh adaption technique for two-dimensional compressible flows on unstructured grids. In *Proceeding of the XIX Congresso Nazionale AIDAA*, Forlì, September 17–21 2007. AIDAA.
 - [29] J. F. Thompson. *Numerical grid generation: foundations and applications*. Elsevier Science Publishing, 1985.
 - [30] A Bagai and J G Leishman. Flow visualization of compressible vortex structures using density gradient techniques. *Exp. Fluids*, 15(6):431–442, 1993.
 - [31] M. P. Scully. Computation of helicopter wake geometry and its influence of rotor harmonic airloads. Report ASR TR178-1, MIT, 1975.
 - [32] G. Fernandez. Implicit Conservative Upwind Schemes for Strongly Transient Flows. Unite de Recherche, INRIA-Sophia Antipolis 873, INRIA, 1988.
 - [33] S. J. Ruuth and W. Hundsdorfer. High-order linear multistep methods with general monotonicity and boundedness properties. *J. Comput. Phys.*, 209:226–248, October 2005.
 - [34] W. Hundsdorfer, S. J. Ruuth, and R. J. Spiteri. Monotonicity-preserving linear multistep methods. *SIAM J. Num. Anal.*, 41(2):605–623, April 2003.
 - [35] L. Tang and J. D. Baeder. Adaptive Euler simulations of airfoil-vortex interaction. *Int. J. Numer. Meth. Fluids.*, 53(5):777–792, 2007.
 - [36] D. Isola. *An Interpolation-Free Two-Dimensional Conservative ALE Scheme over Adaptive Unstructured Grids for Rotorcraft Aerodynamics*. PhD thesis, Politecnico di Milano, 2012.
 - [37] G. R. Srinivasan, W. J. McCroskey, and J. D. Baeder. Aerodynamics of two-dimensional blade-vortex interaction. *AIAA J.*, 24(10), 1986.
 - [38] G. R. Srinivasan, W. J. McCroskey, and J. D. Baeder. Numerical simulations of unsteady airfoil-vortex interactions. *Vertica*, 11(1), 1987.